remote sensing

MDPI

Article

Detecting Water Stress in Winter Wheat Based on Multifeature Fusion from UAV Remote Sensing and Stacking Ensemble Learning Method

He Zhao [1], Jingjing Wang [1], Jiali Guo [1], Xin Hui [1], Yunling Wang [2], Dongyu Cai [3] and Haijun Yan [1,4,*]

[1] College of Water Resources and Civil Engineering, China Agricultural University, Beijing 100083, China; hezhao1023@163.com (H.Z.); jingjingwang_agro@163.com (J.W.); guojl275716606@163.com (J.G.); xin0821h@163.com (X.H.)
[2] College of Animal Science and Technology, Hebei Agricultural University, Baoding 071001, China; 18232050054@163.com
[3] Hebei Science and Technology Innovation Service Center, Shijiazhuang 050051, China; cdongyu@126.com
[4] State Key Laboratory of Efficient Utilization of Agricultural Water Resources, Beijing 100083, China
* Correspondence: yanhj@cau.edu.cn; Tel.: +86-10-62737196

Abstract: The integration of remote sensing technology and machine learning algorithms represents a new research direction for the rapid and large-scale detection of water stress in modern agricultural crops. However, in solving practical agricultural problems, single machine learning algorithms cannot fully explore the potential information within the data, lacking stability and accuracy. Stacking ensemble learning (SEL) can combine the advantages of multiple single machine learning algorithms to construct more stable predictive models. In this study, threshold values of stomatal conductance (g_s) under different soil water stress indices (SWSIs) were proposed to assist managers in irrigation scheduling. In the present study, six irrigation treatments were established for winter wheat to simulate various soil moisture supply conditions. During the critical growth stages, g_s was measured and the SWSI was calculated. A spectral camera mounted on an unmanned aerial vehicle (UAV) captured reflectance images in five bands, from which vegetation indices and texture information were extracted. The results indicated that g_s at different growth stages of winter wheat was sensitive to soil moisture supply conditions. The correlation between the g_s value and SWSI value was high ($R^2 > 0.79$). Therefore, the g_s value threshold can reflect the current soil water stress level. Compared with individual machine learning models, the SEL model exhibited higher prediction accuracy, with R^2 increasing by 6.67–17.14%. Using a reserved test set, the SEL model demonstrated excellent performance in various evaluation metrics across different growth stages (R^2: 0.69–0.87, RMSE: 0.04–0.08 mol m^{-2} s^{-1}; NRMSE: 12.3–23.6%, MAE: 0.03–0.06 mol m^{-2} s^{-1}) and exhibited excellent stability and accuracy. This research can play a significant role in achieving large-scale monitoring of crop growth status through UAV, enabling the real-time capture of winter wheat water deficit changes, and providing technical support for precision irrigation.

Keywords: water stress; soil water stress index; multispectral; stacking ensemble learning

check for updates

Citation: Zhao, H.; Wang, J.; Guo, J.; Hui, X.; Wang, Y.; Cai, D.; Yan, H. Detecting Water Stress in Winter Wheat Based on Multifeature Fusion from UAV Remote Sensing and Stacking Ensemble Learning Method. *Remote Sens.* **2024**, *16*, 4100. https://doi.org/10.3390/rs16214100

Academic Editor: Annamaria Castrignanò

Received: 2 September 2024
Revised: 26 October 2024
Accepted: 29 October 2024
Published: 2 November 2024

Copyright: © 2024 by the authors. Licensee MDPI, Basel, Switzerland. This article is an open access article distributed under the terms and conditions of the Creative Commons Attribution (CC BY) license (https://creativecommons.org/licenses/by/4.0/).

1. Introduction

Wheat, an important global food crop, is grown on more than 200 million hectares [1]. The development and application of irrigation technology have been key factors in increasing wheat yield [2]. Globally, the yield of wheat with sufficient irrigation is 34% more than that of rainfed wheat [3]. Therefore, water stress remains a key factor limiting crop growth and yield. Research has demonstrated that varying water management during different reproductive periods of wheat can significantly affect wheat yield [4]. In many regions, owing to limited natural water resources or inefficient water resource management, crops often face water shortages.

Slight water stress improves the development of wheat populations and increases wheat yields [5]. Therefore, the timely and accurate assessment of water stress conditions is critical for irrigation scheduling. Soil moisture monitoring methods usually include manual sampling and the use of sensors. Manual sampling is a time-consuming and laborious process, while the high cost and limited availability of sensors hinder their use. Moreover, these two methods can only obtain effective data at specific points and are not suitable for large-scale monitoring.

Unmanned aerial vehicles (UAVs) with multispectral camera applications provide new solutions for modern agriculture development [6]. In order to solve the operational problems of crop parameter detection methods, many scholars have used this method to retrieve crop canopy information. For instance, Zhang et al. [7] evaluated the applicability of multispectral imagery under different deficit irrigation levels in maize. Bertalan et al. [8] suggested using UAV-mounted thermal infrared and multispectral data to jointly establish a soil moisture prediction model to improve inversion accuracy. Wang et al. [9] established a chlorophyll fluorescence inversion model using vegetation indices and canopy temperature, which effectively indicates the current water deficit status of crops as an irrigation indicator. Zhang et al. [10] found that UAV multispectral camera resolution influenced canopy structure retention and chlorophyll concentration in response to water stress through vegetation indices showing great sensitivity to maize water stress. UAV multispectral imaging has been widely applied in agriculture, providing critical information for detecting crop water stress and supporting irrigation management in winter wheat [11,12]. Stomatal conductance (g_s) is an important measure of stomatal opening during water and nutrient transport in the soil-plant-atmosphere continuum (SPAC) [13]. As soil moisture content decreases, less water moves upward through the roots, reducing the inhibiting transpiration and g_s. In winter wheat, a sign of drought stress causes a reduction in g_s, which decreases transpiration [14]. Therefore, using g_s as an indicator to detect crop water deficit is feasible. For instance, Wu et al. [15] used g_s as a plant water evaluation standard to adjust the ET model; and Mira-García et al. [16] used g_s as an index of root zone water stress in viticulture. Stomatal conductance serves as a gateway for gas exchange in wheat and has an important effect on yield [17]. Although g_s has been used as a water-sensitive deficit indicator for plants by researchers in existing studies, it is not possible to determine the level of deficit soil moisture by g_s. Most researchers have focused on the flowering and filling stages. However, water management is very important in the whole growth stage of wheat. For example, Liu et al. [18] found that proper water supply at the jointing stage can improve the canopy structure of wheat at the flowering stage and increase the photosynthetic utilization efficiency. Therefore, the aim of this study was to investigate the different fertility stages of wheat and to determine the current soil water deficit level through g_s to support the development of irrigation plans.

Vegetation indices are commonly used in existing studies as a data source for building predictive models. However, when using vegetation indices from multispectral images to identify crop canopies, spectral saturation can be an issue owing to the resolution of optical sensors and near-saturation of the canopy as the plant matures [19]. In addition to obtaining vegetation indices from multispectral images, image texture is a crucial method for expressing crop canopy information. Image texture refers to the arrangement of repeated patterns or colors within an image and is used to describe the visual characteristics and structure of image regions [20]. In the application of UAV remote sensing, image texture can complement vegetation indices. It can improve classification accuracy [21,22], enhance spatial resolution [23,24], and provide better adaptability to complex environments [25,26].

With the development of modern data processing techniques, machine learning has gained popularity in agriculture because of its strong ability to capture nonlinear relationships [27,28]. Research has been conducted to apply machine learning to agriculture. For instance, Wang et al. [29] showed that a gradient-boosting decision tree (GBDT) exhibits better accuracy in wheat g_s prediction compared with a support vector machine (SVM). Zhou et al. [30] reported that a backpropagation neural network (BPNN) exhibits higher

prediction accuracy compared with an extreme learning machine (ELM) in constructing a wheat g_s prediction model. Pei et al. [31] reported that the extreme gradient boosting (XGBoost) method exhibited better overall performance at the canopy scale. However, single machine learning algorithms cannot fully explore the potential information within the data, lacking stability and accuracy. These drawbacks limit the widespread diffusion and use of predictive modeling as well as of machine learning in agriculture. In remote sensing inversion models that use g_s as an indicator of water deficit, single machine learning algorithms are commonly used. Stacking ensemble learning (SEL), which originated from machine learning, aims to improve prediction accuracy while reducing generalization errors by constructing and combining multiple predictive models. Tao et al. [32] established a root zone moisture prediction model using seven features, including surface temperature and evaporation. It was found that the SEL can achieve higher prediction accuracy by taking advantage of different machine learning algorithms. Jiang et al. [33] concluded that the performance of an integrated model was significantly influenced by the combination of the basic learners. An optimal combination strategy can significantly improve prediction model accuracy. Zhai et al. [34] established a multifeature dataset using multispectral, thermal infrared, and visible light characteristics. They employed the SEL model, which significantly improved chlorophyll prediction accuracy. SEL models can more effectively handle data imbalance and combine the advantages of different models, enhancing tolerance to dataset noise [35]. Moreover, few studies have combined multispectral and image texture information as input features for the model. Therefore, in this study, the vegetation index and image texture were used as data sources, and an SEL model was used to establish the prediction model of g_s and to obtain the g_s thresholds under different soil water stress indices (SWSIs). The g_s threshold can be used to determine the current SWSI levels more easily, which is convenient for agricultural managers to develop a more scientific irrigation program.

Therefore, this study employed g_s as a water stress indicator and integrated multispectral and textural information from a UAV into a dataset to develop a comprehensive winter wheat water stress diagnostic model using a two-layer SEL model. The major research objectives of this study were to (1) obtain the relationship between the g_s response of winter wheat to different water stress environments and determine the threshold value of g_s under different water stress levels at different growth stages, (2) compare the performance of SEL and single machine learning in building g_s prediction models, and (3) validate the SEL model through the reserved test set in order to evaluate the accuracy of the model in a new dataset environment.

2. Materials and Methods

2.1. Overview of the Experimental Site

The experiment was conducted at the Hebei Science and Technology Innovation Service Center (37.93°N, 114.43°E) in Hebei Province, China (Figure 1). The experimental station is located in the pre-mountain plains of the Taihang Mountains in the North China Plain, with an average elevation of 69 m, an average temperature of 13.7 °C, and an average annual rainfall of 604.7 mm. The main crops in this region are winter wheat and summer corn. The soil is loamy sand (as defined by the soil texture triangle) [36]. The field capacity (FC) was 0.34 cm^3 cm^{-3} (0–40 cm average soil layer) and wilting point (WP) was 0.04 cm^3 cm^{-3} (0–40 cm average soil layer). Before sowing, soil samples from the 0–100 cm layer were collected, and their physical and chemical properties were analyzed. The soil organic matter content, available phosphorus, nitrate nitrogen, ammonium nitrogen, and exchangeable potassium contents were measured as 0.17%, 23.4 mg kg^{-1}, 32.2 mg kg^{-1}, 10.58 mg kg^{-1}, and 55.0 mg kg^{-1}.

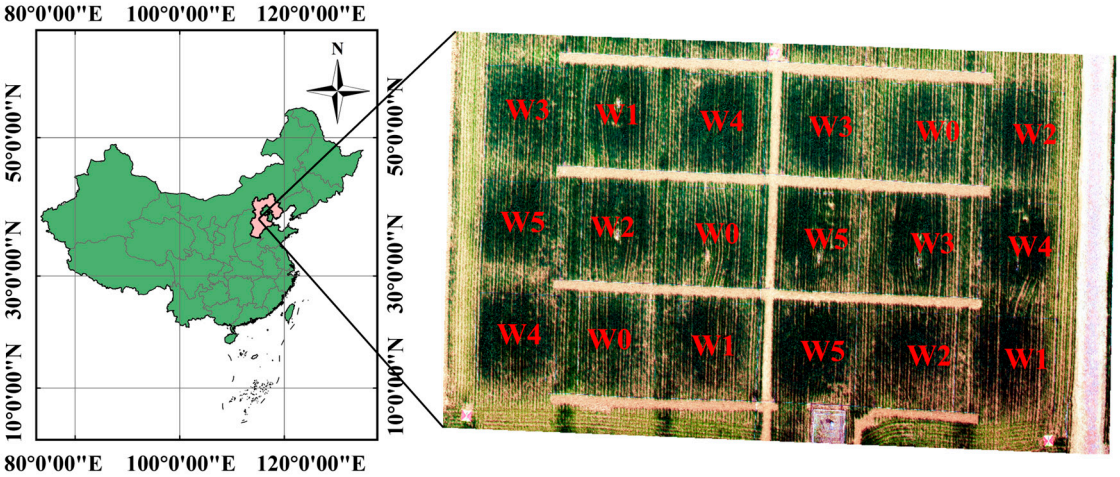


Figure 1. Location of the study area and the experimental treatments. Note: W0–W5 represent different irrigation levels.

2.2. Experimental Design

The experiment was conducted in 2022 and 2023, using the winter wheat variety "Jinhe 9123". Before sowing, nitrogen, phosphorus, and potassium fertilizers were uniformly applied as base fertilizers (N 220 kg hm^{-2}, P 102 kg hm^{-2} and K 60 kg hm^{-2}). The winter wheat experiment included six irrigation levels: W0, W1, W2, W3, W4, and W5. The W4 treatment served as the control group, with its irrigation amount designated as I. The irrigation amounts for the W1, W2, W3, and W5 treatments were 40%I, 60%I, 80%I, and 120%I, respectively. W0 was a rainfed treatment. The amount of irrigation water was controlled by the upper and lower soil moisture limits. Irrigation was performed when the average soil moisture content within the planned wetting depth for the W4 treatment reached the set lower limit and proceeded to the upper limit. The lower limit of irrigation was 65–70% of the FC, and the upper limit was 90% of the FC. Before flowering, the planned wetting depth was 0–40 cm. After the flowering stage, the planned wetting depth was 0–60 cm.

Each water irrigation level was set with three replicates and was completely randomized, resulting in 18 plots. The experimental plots were 8 m × 8 m, with a 2 m isolation strip between each plot. The sprinkler head type was a linear rotary (MP3000, Hunter Industries Inc., San Marcos, TX, USA), with stable working pressure and uniform water output. The sprinkler heads were arranged in a fixed sprinkler irrigation setup, with the four corners of the test area installed in a four-corner arrangement, and each nozzle sprayed at 90°. A gate valve and pressure gauge were installed at the head of each plot. During irrigation, the valve was adjusted to maintain the pipeline pressure at 0.2 MPa, providing a combined application rate of 10 mm/h. The irrigation water volume was controlled by adjusting the irrigation time.

2.3. UAV Image Acquisition

2.3.1. UAV Remote Sensing Platform

The UAV platform used was a DJI Phantom 4 RTK (DJI Sciences and Technologies Ltd., Shenzhen, China) (Figure 2). The multispectral camera was mounted on the UAV using a 3D-printed bracket and was powered by a portable power source. The flights were conducted in sunny weather with low wind speeds. The flight time was between 11:00 and 14:00. Flight altitude was set at 30 m. The flight overlap was set to 80% for longitudinal overlap and 75% for lateral overlap. Five ground control points (GCPs) were established in the test area. The precise positions of the GCPs were determined by a RTK GNSS receiver (M600 mini, ComNav Technology Ltd., Shanghai, China). The RTK program used was Qianxun Find CM (Qianxun Spatial Intelligence Inc., Shanghai, China), which had an accuracy of 1 cm. Table 1 shows the flight times and conditions during the study.



Figure 2. The UAV platform and multispectral camera.

Table 1. Flight time of the UAV and the corresponding meteorological parameters.

Growth Stage	2022					2023				
	Date	Ta °C	RH %	RS W·m^{-2}	WS m·s^{-1}	Date	Ta °C	RH %	RS W·m^{-2}	WS m·s^{-1}
Revival	7 April 2022	20.8	45.3	400.9	1.7	26 March 2023	14.8	36.6	453	0.5
Jointing	15 April 2022	17.1	27.9	433.9	1.6	14 April 2023	21.8	44.9	214	1.0
Heading	20 April 2022	26.9	33.0	516.4	1.2	27 April 2023	14.9	63.7	399.3	1.2
Flowering	3 May 2022	32.6	33.4	572.6	1.1	7 May 2023	23.8	33.5	882	1.3
Filling	24 May 2022	30.5	45.4	657.7	0.6	22 May 2023	26.8	30.4	976	0.6

Note: Ta is the air temperature (°C); RH is the relative humidity (%); RS is the solar radiation (W m^{-2}); WS is the wind speed (m s^{-1}).

2.3.2. Multispectral Information Acquisition

The multispectral camera (MicaSense Red Edge-MX, AgEagle Aerial Systems Inc., Wichita, KS, USA) had an image resolution of 1280 × 960 pixels (Figure 2). It can simultaneously collect spectral bands in the blue, green, red, red edge, and near-infrared spectra. The bands are 475, 560, 668, 842, and 717 nm, respectively. The total number of pixels in the multispectral camera was six million, with 1.2 million pixels per band. The capture rate for all the channels was set to once per second. Radiometric calibration was performed before each flight (calibration of reflective panels, CRP, and MicaSense). The camera shooting interval was set to 2 s.

2.3.3. Data Processing

The multispectral images were corrected and stitched using Pix4D Mapper (Pix4D 4.5.2, Pix4D S.A., Lausanne, Switzerland). Position and radiometric corrections were performed using GCP control points and radiometric panels. The stitched images were then processed in QGIS 3.26 to extract radiometric data for each experimental plot. These reflectance values were used to calculate 26 common vegetation indices (Table 2). The OTSU threshold method was used to differentiate between vegetation and soil backgrounds [37]. The zonal statistics function was then used to extract the vegetation index value for each plot.

Texture information of the image was obtained using Gray Level Co-occurrence Matrix (GLCM) [38]. Eight texture measurements based on GLCM were calculated using ENVI 5.3, including Mean (MEA), Variance (VAR), Homogeneity (HOM), Contrast (CON), Dissimilarity (DIS), Entropy (ENT), Second Moment (SEC), and Correlation (COR) (Figure 3).

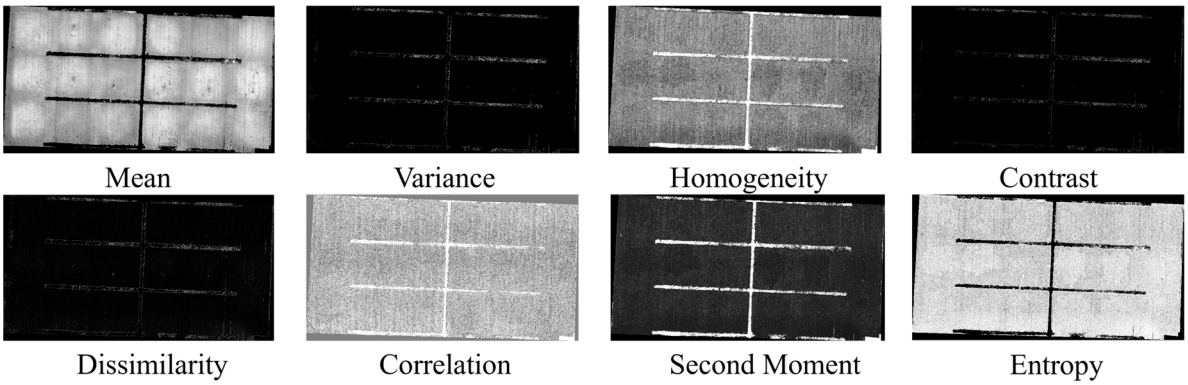


Figure 3. Image texture type.

Table 2. Equations for vegetation indices.

Vegetation Indices	Formula	References
Normalized difference vegetation index, *NDVI*	$NDVI = (NIR - R)/(NIR + R)$	[39]
Green normalized difference vegetation index, *GNDVI*	$GNDVI = (NIR - G)/(NIR + G)$	[40]
Enhanced vegetation index, *EVI*	$EVI = 2.5 \times (NIR - R)/(NIR + 6R - 7.5B + 1)$	[41]
Enhanced vegetation index 2, *EVI2*	$EVI2 = 2.5 \times (NIR - R)/(NIR + 2.4R + 1)$	[42]
Soil-adjusted vegetation index, *SAVI*	$SAVI = (NIR - RR/(NIR + R + 0.5) \times 1.5$	[43]
Optimized soil-adjusted vegetation index, *OSAVI*	$OSAVI = 1.16 \times (NIR - R)/(NIR + R + 0.16)$	[44]
Green optimal soil-adjusted vegetation index, *GOSAVI*	$GOSAVI = 1.16 \times (NIR - G)/(NIR + G + 0.16)$	[45]
Modified chlorophyll absorption in reflectance index, *MCARI*	$MCARI = [(RE - R) - 0.2 \times (RE - G)] \times (RE/R)$	[46]
MCARI/OSAVI	*MCARI/OSAVI*	[47]
Modified simple ratio, *MSR*	$MSR = (NIR/R - 1)/[(NIR/R)^{0.5} + 1]$	[48]
Structure insensitive pigment index, *SIPI*	$SIPI = (NIR - B)/(NIR/RB)$	[49]
Red-edge normalized difference vegetation index, *NDRE*	$NDRE = (NIR - RE)/(NIR + RE)$	[50]
Green ratio vegetation index, *GRVI*	$GRVI = NIR/G$	[51]
Ratio vegetation index, *RVI*	$RVI = NIR/R$	[52]
Excess green, *EXG*	$EXG = 2 \times G - B - R$	[27]
Red-edge chlorophyll index, *CIRE*	$CIRE = (NIR/RE) - 1$	[53]
Difference vegetation index, *DVI*	$DVI = NIR - R$	[54]
MERIS terrestrial chlorophyll index, *MTCI*	$MTCI = (NIR - RE)/(RE - R)$	[55]
Modified triangular vegetation index 2, *MTCI2*	$MTCI2 = 1.5 \times [1.2 \times (NIR - G) - 2.5 \times (R - G)]/\sqrt{2 \times (NIR + 1)^2 - 6 \times NIR + 5 \times R^{0.5} - 0.5}$	[48]
Normalized difference vegetation index red-edge, *NDVIRE*	$NDVIRE = (NIR - RE)/(NIR + RE)$	[56]
Nonlinear vegetation index, *NLI*	$NLI = (NIR \times NIR - R)/(NIR^2 + R)$	[57]
Plant pigment ratio, *PPR*	$PPR = (G - B)/(G + B)$	[58]
Re-normalized difference vegetation index, *RDVI*	$RDVI = (NIR - R)/\sqrt{(NIR + R)}$	[59]
Nitrogen reflectance index, *NRI*	$NRI = (G - R)/(G + R)$	[60]
Transformed chlorophyll absorption ratio index, *TCARI*	$TCARI = 3\,[(RE - R) - 0.2 \times (RE - RG) \times RE/R]$	[61]
Triangular vegetation index, *TVI*	$TVI = 0.5 \times [120 \times (NIR - G) - 200 \times (R - G)]$	[62]

Note: *NIR*, *RE*, *R*, *G*, and *B* are reflectance values of wheat in near-infrared, red-edge, red, green, and blue bands, respectively, from the multispectral camera.

2.4. Ground Data Acquisition

2.4.1. Stomatal Conductance

On the day of the UAV data collection, the g_s of winter wheat was measured using a porometer (SC-1, METER Group, Inc., Washington, DC, USA). Two Regions of Interest (ROI) were set up within each water treatment plot, and three representative plants were selected within each ROI to measure g_s. The top leaves of the wheat plants were selected for measurement before the heading stage, and the flag leaves were selected after the heading stage. The g_s measurements were taken between 11:00 and 14:00. Before the

measurement, the desiccant in the porometer was replaced, and the device was calibrated using a standard reagent.

2.4.2. Soil Water Content

Soil water content (SWC) was monitored using a TDR device (Trime-T3, Ettlingen, Germany). A Trime tube was installed at the center of each plot. SWC at 0–40 cm soil depth was measured after each flight. The TDR measurements were calibrated before the experiment using the soil extraction and drying method.

2.4.3. Meteorological Parameters

A weather station (HOBO U30, Onset Computer Corporation, Bourne, MA, USA) was set up at the experimental site to record data such as wind speed, temperature, relative humidity, and solar radiation during the UAV flight.

2.4.4. Calculation of Water Deficit Indices

The soil water stress index (SWSI) was calculated based on the available SWC that crops can utilize [63].

$$SWSI_i = \frac{SWC_i - WP}{FC - WP}. \quad (1)$$

SWC_i represents the soil water content in different experimental plots. The soil texture across the plots was uniform, with an FC of 0.34 cm^3 cm^{-3} and a WP of 0.04 cm^3 cm^{-3}.

2.5. Stacking Ensemble Learning Model Construction and Evaluation

2.5.1. Stacking Ensemble Learning Model

SEL is a hierarchical model framework that integrates the outputs of multiple base models to optimize performance and generalization ability, addressing the limitations of a single base model [35]. The training of the basic machine learning is the first layer. The outputs are used as inputs for the second layer, and the final prediction results are obtained [64]. The basic process of this algorithm is shown in Figure 4. To avoid overfitting, K-fold cross-validation is often used to ensure that all the data are involved in the training. This paper uses 3-fold cross-validation.

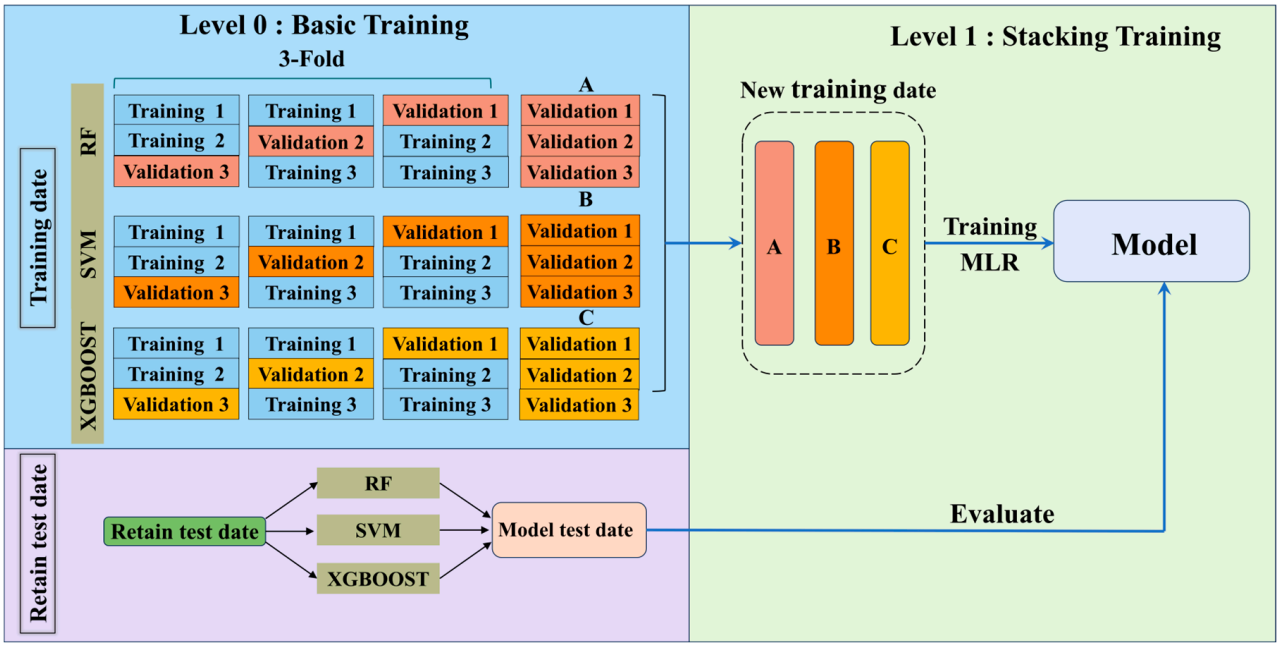


Figure 4. Stacking ensemble learning model.

The steps to construct the SEL model were as follows (Figure 4):

(1) The data were divided into training and reserved test sets in a 3:1 ratio.
(2) The training set was input into different base learners at Level 0 for separate training. Based on 3-fold cross-validation, the training set was divided into three parts, and each part was used as a validation set. New feature vectors (A, B, and C) were generated as the base learners predicted each fold in the training set.
(3) The predicted values output from the different base learners from the new training data, which were used to train Level 1 learners. These learners then outputted the final prediction results.
(4) Validated SEL model results using the retained test set.

2.5.2. Basic Models

Herein, the base learners at Level 0 comprised random forest (RF), SVM, and XGBoost models, whereas the Level 1 learner was the mixed logistic regression (MLR) algorithm. The hyperparameters of each base model were tuned using the grid search method. The RF, SVM, XGBoost, and MLR models were implemented using the sklearn package in Python 3.6 [65].

RF is a decision tree-based machine learning algorithm proposed by Breiman [66]. The core concept is nesting in integrated learning, which involves retrieving and training N parts from a dataset. Parallel training was performed between the two parts. These parts are combined to form a "forest", and the final result is obtained by a "voting" method [15]. The RF algorithm is widely recognized for its broad application range, minimal parameter tuning, high accuracy, and strong capability to manage high-dimensional feature spaces [67]. SVM is a supervised machine learning algorithm. In contrast to support vector regression (SVR), SVM focuses on constructing one or more hyperplanes in a high-dimensional or infinite-dimensional space to maximize the minimum distance between the hyperplane and the sample points. Herein, the radial basis function was used as the SVM kernel function because of its ability to approximate any nonlinear function and its fast learning convergence rate. XGBoost, an efficient and widely used tree-boosting method, is based on GBDT [68]. The core idea of XGBoost is to combine the advantages of tree models within a gradient-boosting framework by iteratively training multiple decision tree models and merging them into a powerful ensemble model. The XGBoost algorithm is widely recognized for its excellent performance, flexibility, and accuracy. The MLR algorithm is a classic machine learning algorithm with a core idea that fits a linear model to describe the relationship between independent and dependent variables, where the independent variables can be one or more continuous or categorical variables. MLR is a commonly used and effective model, providing reliable prediction results.

2.5.3. Statistical Analysis

To assess the reliability and accuracy of the model, this study employed the coefficient of determination (R^2), root mean square error (RMSE), normalized root mean square error (NRMSE), and mean absolute error (MAE) as evaluation criteria. The formulas for these calculations are as follows:

$$R^2 = 1 - \frac{\sum_{i=1}^{n}(y_i - \hat{y}_i)^2}{\sum_{i=1}^{n}(y_i - \overline{y_i})^2} \quad (2)$$

$$RMSE = \sqrt{\frac{1}{n}\left(\sum_{i=1}^{n}(y_i - \hat{y}_i)^2\right.} \quad (3)$$

$$NRMSE = \frac{\sqrt{\frac{1}{n}\sum_{i=1}^{n}(y_i - \hat{y}_i)^2}}{\hat{y}} \times 100\% \quad (4)$$

$$MAE = \frac{1}{n}\sum_{i=1}^{n}\left|\hat{y_i} - y_i\right|. \quad (5)$$

where $\hat{y}_i$ is the output value of the model of g_s, y_i is the observed value of g_s, $\overline{y}$ is the average observed value of g_s, and n is the number of samples.

3. Results

3.1. Statistics of Stomatal Conductance of Wheat Under Different Water Deficit Treatments

Figure 5 shows the changes in g_s throughout the wheat growing stages in 2022 and 2023. In 2022, g_s ranged from 0.11 to 0.62 mol m^{-2} s^{-1}, while in 2023, it ranged from 0.08 to 0.64 mol m^{-2} s^{-1}. Data from the two years showed a similar trend: g_s gradually increased from the revival stage, peaking at the jointing and heading stages, and then gradually decreased during the flowering and filling stages. The performance of g_s under different water supply conditions varied across the fertility periods. The differences in g_s during the jointing and filling stages were the most significant. This may be due to the fact that these stages correspond to the peak of growth and reproductive development of winter wheat with higher water requirements. This led to significant differences in g_s among the different treatments. In particular, in the rainfed control group (W0), the decreasing trend in g_s was especially noticeable throughout the wheat growth stage because of the prolonged lack of irrigation. This suggests that g_s is dynamic under different water supply conditions and under different fertility periods. The water deficit could not be expressed using the same g_s threshold over the whole wheat reproductive period.

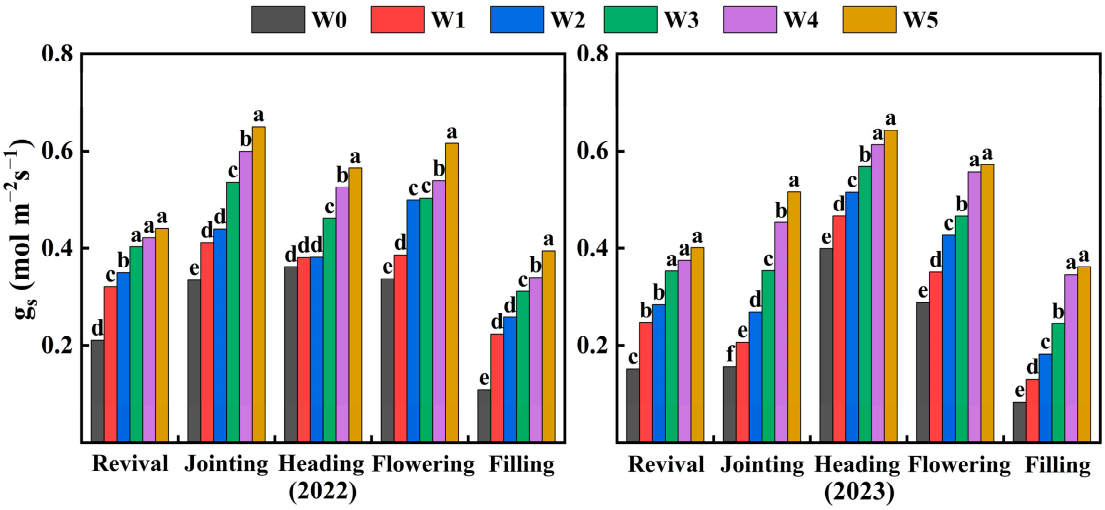


Figure 5. Stomatal conductance (g_s mol m^{-2} s^{-1}) of wheat at the revival, jointing, heading, flowering, and filling stages in 2022 and 2023. Note: Different lowercase letters indicate significant differences in stomatal conductance at a p value of <0.05.

3.2. Soil Water Stress Index of Wheat at Different Growth Stages

Figure 6 shows the SWSI during the revival, jointing, heading, flowering, and filling stages for 2022 and 2023. The SWSI ranged from 0.45 to 0.95 in 2022 and from 0.37 to 0.95 in 2023. Significant differences ($p < 0.05$) in the SWSI were observed under different irrigation treatments. The SWSI range remained consistent over the 2-year study period, providing a broad and stable dataset that would improve the stability of the model.

The differences in the SWSI varied at different fertility stages. In the 2022 and 2023 experiments, the difference in the SWSI between treatments was the smallest at the jointing stage, with differences of 0.26 and 0.22, respectively. The differences in the SWSI were the largest at the filling and flowering stages, reaching 0.34 and 0.49, respectively. This phenomenon was attributed to the filling and flowering stages being the period of most active growth in wheat, when water is consumed more rapidly from the soil, resulting in smaller differences in the SWSI among treatments. With different irrigation treatments, the differences in the SWSI increased and reached a maximum during the filling and flowering stages.

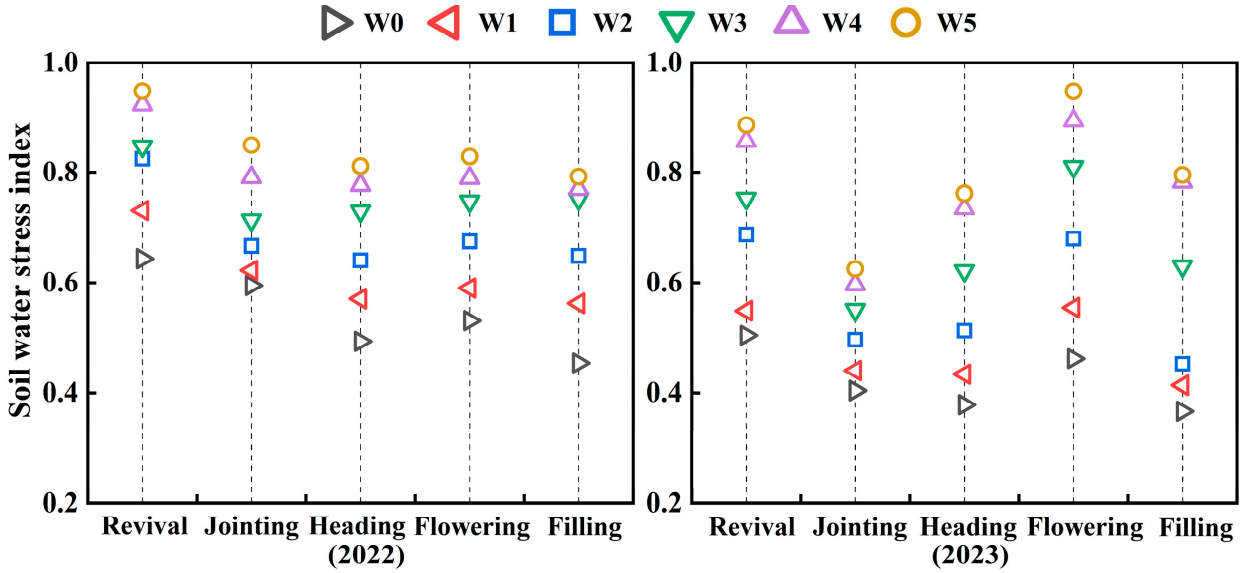


Figure 6. Soil water stress index of wheat at the revival, jointing, heading, flowering, and filling stages in 2022 and 2023.

3.3. Relationship Between Stomatal Conductance and Soil Water Stress Index of Wheat

To further explore the relationship between the SWSI and g_s, we constructed a fitting model using data from the various growth stages of wheat in 2022 and 2023. The fitting accuracy between the SWSI and g_s during the revival, jointing, heading, flowering, and filling stages was good, with corresponding R^2 values of 0.84, 0.80, 0.89, 0.79, and 0.86. The fitting formulas for each growth stage are also provided in Figure 7, demonstrating a clear linear relationship between the SWSI and g_s. Stomatal conductance is a continuous channel between the soil water potential and atmosphere of plants. When soil water potential decreases, soil root resistance increases, and water transport channels in plants begin to hollow out. In order to curb this phenomenon and reduce water loss, stomata are gradually closed [69]. This point was also proven in the experiment by Asargew et al. [70], which showed that the degree of soil water stress was linearly related to stomatal conductance. Therefore, we can evaluate the current soil water stress status of wheat by measuring its current g_s, indirectly validating the feasibility of using g_s as an effective indicator of soil water stress. It is worth noting that the fitting accuracy and equations differed for different growth stages. This may be due to the combined effect of biological characteristics and different irrigation strategies at each fertility stage.

Using g_s to assess wheat water deficit status allows for classification based on g_s values. According to existing research, the soil volumetric water content for different stress levels should be maintained at less than 50%, 50–60%, 60–70%, 70–80%, and more than 80% of the FC, respectively [71]. The SWSI was calculated based on FC under different soil water stress conditions: extreme drought (SWSI < 0.43), severe water stress (SWSI: 0.43–0.55), moderate water stress (SWSI: 0.55–0.66), slight water stress (SWSI: 0.66–0.77), and no water stress (SWSI > 0.77). Based on the equation established in the previous section between g_s and the SWSI, the value of g_s could be determined for each growth stage and soil moisture stress levels. Table 3 shows the g_s values of winter wheat at various growth stages under different stress levels.

Table 3. Threshold ranges of g_s at different growth stages.

Growth Stage	Fitting Relation	Extreme Deficit	Severe Deficit	Moderate Deficit	Slight Deficit	No Deficit
Revival	y = 0.59x − 0.11	<0.14	0.14–0.21	0.21–0.28	0.28–0.34	>0.34
Jointing	y = 0.89x − 0.14	<0.24	0.24–0.35	0.35–0.45	0.45–0.55	>0.55
Heading	y = 0.60x − 0.89	<0.16	0.16–0.23	0.23–0.3	0.30–0.36	>0.36
Flowering	y = 0.53x − 0.12	<0.11	0.11–0.17	0.17–0.23	0.23–0.29	>0.29
Filling	y = 0.56x − 0.10	<0.14	0.14–0.21	0.21–0.27	0.27–0.33	>0.33

Note: x represents the SWSI threshold range, and y represents the stomatal conductance (g_s) threshold range (mol m^{-2} s^{-1}).

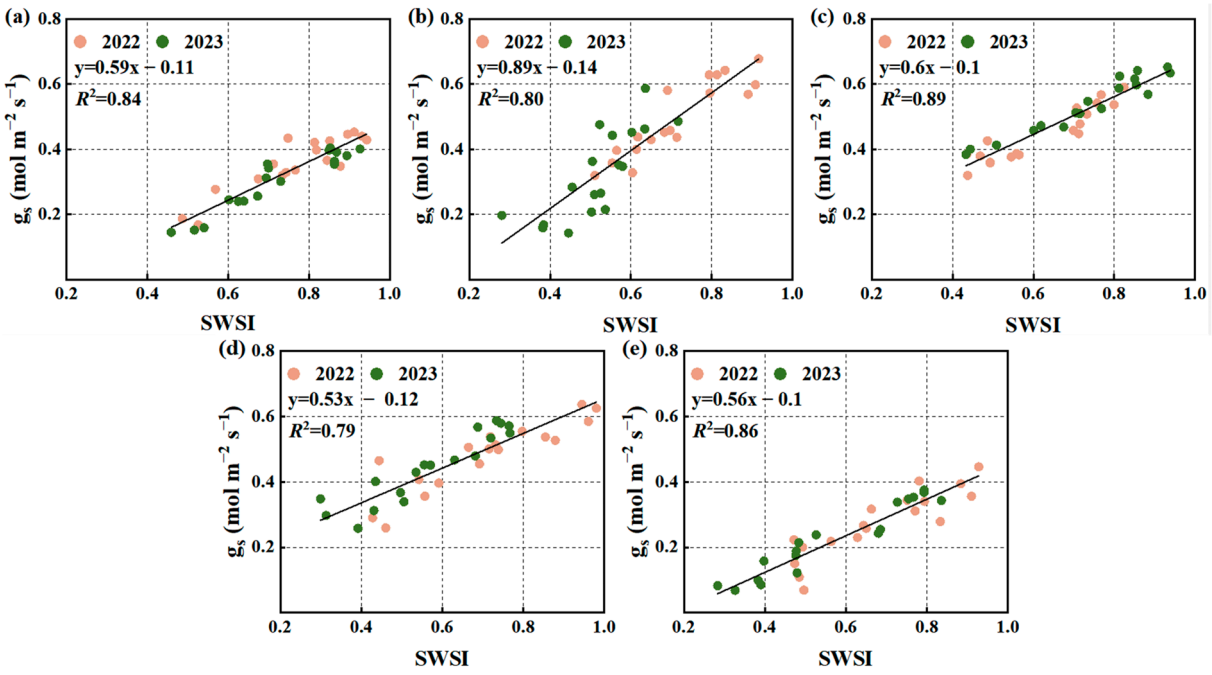


Figure 7. Fitting relationship between soil water stress index and g_s in 2022 and 2023. Note: (**a**) Revival stage. (**b**) Jointing stage. (**c**) Heading stage. (**d**) Flowering stage. (**e**) Filling stage.

3.4. Relationship Between Stomatal Conductance, Vegetation Indices, and Image Texture

Pearson correlation analysis was performed between the vegetation indices and g_s. The matrix of correlation coefficients (correlation coefficient r) is shown in Figure 8. In the 2-year experiments, all the vegetation indices except *TCARI* and *SIPI* showed a positive correlation with g_s, whereas *TCARI* and *SIPI* showed a negative correlation with g_s.

Stomatal conductance reflects the degree of stomatal opening in plants, which affects the water transpiration rate and carbon dioxide absorption. High stomatal conductance usually means that the plant has a better water status, strong transpiration, strong carbon dioxide absorption capacity, and more active photosynthesis. Different water states affect the plant population development, photosynthetic intensity, and chlorophyll content, which in turn affect the plant characteristics under different reflectance.

The correlation was weak during the revival stage and reached a high level during the flowering and filling stages, with a gradually increasing trend. Based on the correlation analysis of g_s and the multispectral vegetation indices over 2 years, the five vegetation indices with the highest correlation at each growth stage were selected as the basic models and the SEL model's input dataset. For the revival stage, *NDVI*, *GNDVI*, *MSR*, *SIPI*, and *TCARI* were selected. For the jointing stage, *SAVI*, *OSAVI*, *GRVI*, *RDVI*, and *NRI* were selected. For the heading stage, *GOSAVI*, *MSR*, *RVI*, *CIRE*, and *TCARI* were selected. For the flowering stage, *GNDVI*, *NDRE*, *CIRE*, *MERIS MTCI*, and *NDVIRE* were selected. For

the filling stage, *GNDVI*, *MSR*, *RVI*, *NRI*, and *TCARI* were selected. For the whole growth stage, *MCARI*, *MSR*, *GRVI*, *MTCI2*, and *NRI* were selected.

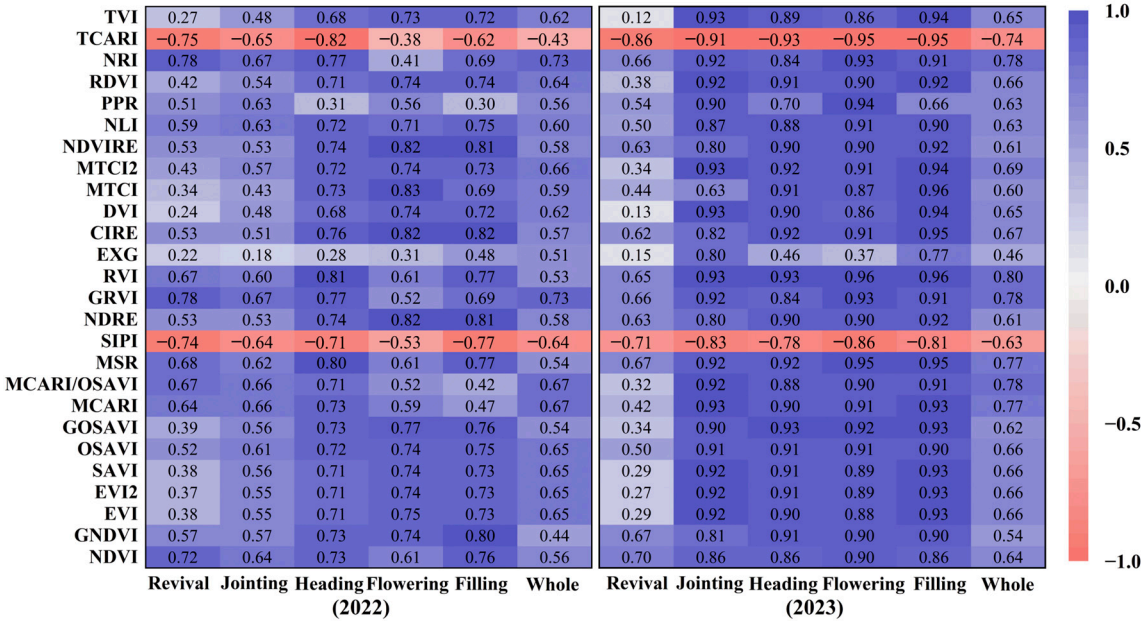


Figure 8. Pearson correlation coefficient between stomatal conductance (g_s) and vegetation indices (VIs). Note: Revival represents the wheat revival stage; Jointing represents the wheat jointing stage; Heading represents the wheat heading stage; Flowering represents the wheat flowering stage; Filling represents the wheat filling stage; Whole represents the whole growth stage of the wheat.

Image texture features reflect the change mode of pixel gray value in the image, and these features can reflect the microstructure of plant leaves. Different levels of water supply will affect the changes in the canopy structure of the wheat population, resulting in differences in image texture. Eight texture indices, namely MEA, VAR, HOM, CON, DIS, ENT, SEC, and COR, were extracted from the spectral images of each band of the multispectral images obtained by the UAV. The histograms in Figure 9 represent the performance of different image textures from various multispectral bands in correlation with g_s at different growth stages, using different colors and lengths. Unlike most vegetation indices, not all image textures are strongly correlated with g_s. Each band's texture information performed differently at various growth stages; for instance, the green band texture was sensitive to g_s during the revival stage, the red-edge band during the jointing stage, and the red band after the heading stage. Moreover, different image textures showed varying degrees of sensitivity to g_s. For example, MEA from different bands responded relatively sensitively to g_s across different growth stages. Certain texture types from specific bands were also sensitive to g_s. For instance, COR from the red band exhibited a high correlation with g_s after the heading stage. The five image textures with the highest correlation for each period were selected as the model input dataset (Table 4).

Table 4. Image textures selected for different growth stages.

Growth Stage	Image Texture
Revival	G-CON, G-DIS, R-MEA, R-VAR, R-DIS
Jointing	G-ENT, RE-HOM, RE-DIS, RE-ENT, RE-SM
Heading	B-COR, G-MEA, R-MEA, R-HOM, R-COR
Flowering	B-MEA, B-COR, N-COR, R-MEA, R-COR
Filling	N-MEA, R-MEA, R-HOM, R-DIS, R-COR
Whole	N-SM, R-MEA, R-HOM, R-DIS, R-ENT

Note: Taking G-Con as an example, it represents the Con texture in the green band of the multispectral image. Whole represents the whole growth stage of the wheat.

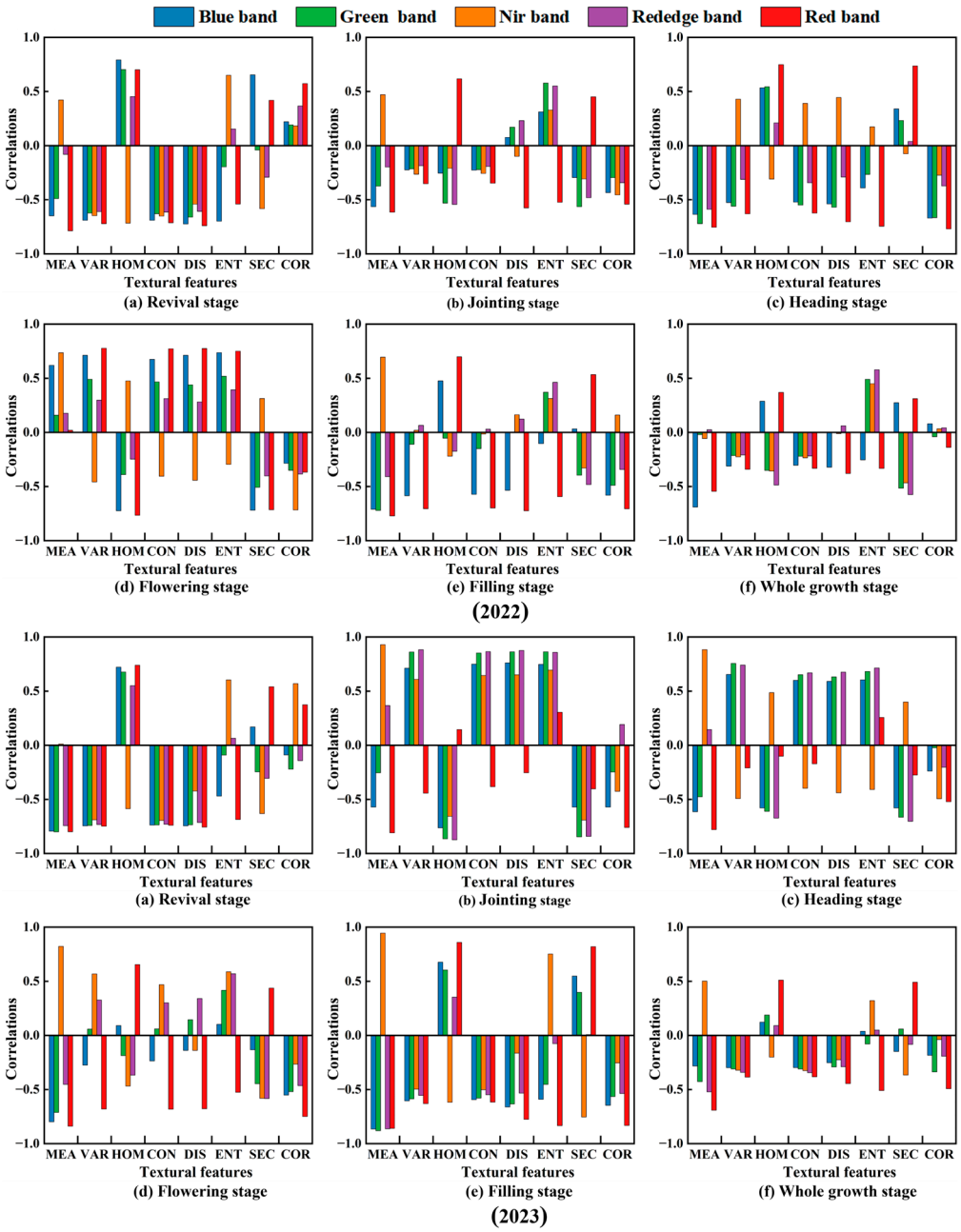


Figure 9. Pearson correlation coefficient of image texture and stomatal conductance (g_s) at each growth stage in 2022 and 2023. Note: (**a**) Revival stage. (**b**) Jointing stage. (**c**) Heading stage. (**d**) Flowering stage. (**e**) Filling stage. (**f**) Whole wheat growth stage.

3.5. Results of Stomatal Prediction by Different Models

Figure 10 shows the simulation results of the first-layer learning models RF, SVM, and XGBoost, and the data simulation results of the second-layer MLR learning model. Among the growth stages, the simulation accuracy of the SEL model was the highest during the heading stage and the lowest during the jointing stage.

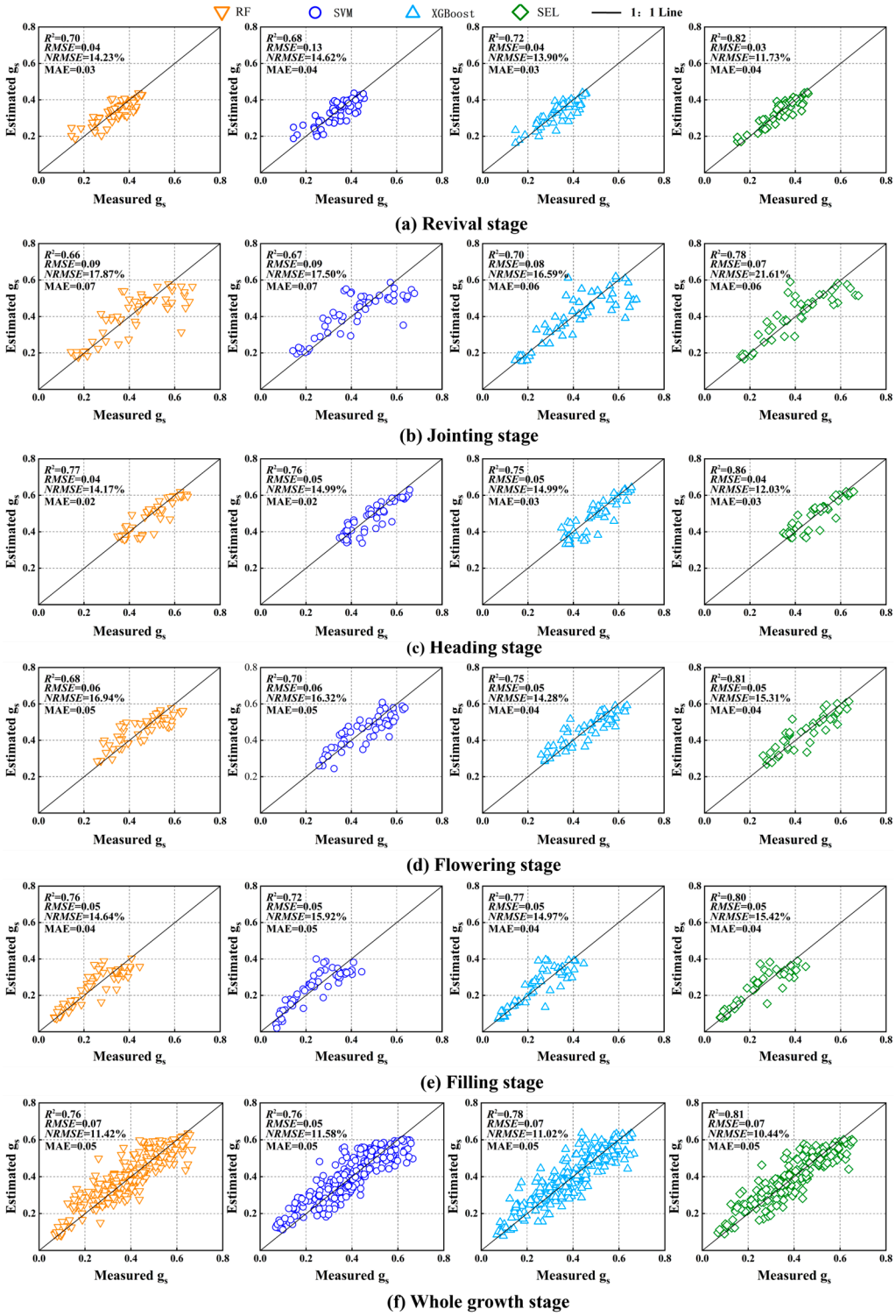


Figure 10. Estimation of g_s accuracy based on RF, SVM, XGBoost, and SEL models. Note: (**a**) Revival stage. (**b**) Jointing stage. (**c**) Heading stage. (**d**) Flowering stage. (**e**) Filling stage. (**f**) Whole wheat growth stage.

Among the three basic learners, the XGBoost model showed varying degrees of improvement in simulation accuracy compared to the RF and SVM models. Except for the heading stage, the RF model was more accurate. This variation is typical when building machine learning models. It is improbable that a single model consistently yields optimal results across varying environments, highlighting the advantages of SEL models. As shown in Figure 10, the SEL model outperformed the base learners across different growth stages,

with R^2 improvements ranging from 6.25% to 14.63%. The simulation accuracy for g_s varied among stages, with the highest accuracy during the heading stage (SEL-R^2 = 0.86) and the lowest during the jointing stage (SEL-R^2 = 0.78). The g_s prediction for the whole growth period is shown in Figure 10f. Compared with the base learners, the SEL model significantly improved g_s prediction accuracy over the whole growth period (R^2 = 0.81, RMSE = 0.07 mol m^{-2} s^{-1}, and NRMSE = 10.44%).

The accuracy of the SEL model was evaluated with the retained test set. As Table 5 shows, the prediction accuracy R^2 values of the SEL model for g_s at different growth stages were larger than 0.78. The SEL model effectively addressed the instability in prediction accuracy associated with single learners. For example, during the jointing stage, the XGBoost model, which generally performed well, achieved an R^2 of 0.446, whereas the SEL model achieved an R^2 of 0.757. The prediction accuracy of the SEL model for g_s throughout the growth period was 0.806. This indicates that the SEL model was suitable for predicting g_s throughout the growth period.

Table 5. Retaining the test set for g_s accuracy estimates based on RF, SVM, XGBoost, and SEL models.

Growth Stage	Model	R^2	RMSE (mol m^{-2} s^{-1})	NRMSE (%)	MAE (mol m^{-2} s^{-1})
Revival	RF	0.740	0.062	22.8	0.049
	SVM	0.785	0.061	25.6	0.048
	XGBoost	0.774	0.057	21.6	0.043
	SEL	0.798	0.053	19.7	0.042
Jointing	RF	0.688	0.077	19.7	0.061
	SVM	0.446	0.103	22.4	0.047
	XGBoost	0.701	0.076	21.4	0.089
	SEL	0.757	0.076	23.6	0.056
Heading	RF	0.720	0.049	21.5	0.037
	SVM	0.678	0.052	18.7	0.036
	XGBoost	0.737	0.046	18.8	0.041
	SEL	0.799	0.041	17.5	0.033
Flowering	RF	0.516	0.065	27.4	0.057
	SVM	0.492	0.063	25.1	0.045
	XGBoost	0.655	0.052	19.8	0.052
	SEL	0.688	0.049	21.0	0.039
Filling	RF	0.727	0.050	19.6	0.044
	SVM	0.807	0.044	16.6	0.037
	XGBoost	0.813	0.041	15.4	0.038
	SEL	0.867	0.039	16.2	0.036
Whole	RF	0.763	0.073	17.4	0.055
	SVM	0.761	0.080	17.5	0.058
	XGBoost	0.780	0.069	14.7	0.051
	SEL	0.806	0.063	12.3	0.046

Note: Whole represents the whole growth stage of the wheat.

4. Discussion

4.1. Changes in g_s and Threshold Ranges of Winter Wheat Under Different Water Supply Conditions

Stomatal conductance is one of the earliest indicators of changes in plants when water is scarce. After absorbing water from the soil, plants release water into the atmosphere through transpiration to facilitate water and nutrient transport from the roots to stems and leaves. Under water deficit conditions, stomatal conductance decreases rapidly, and this feedback mechanism can significantly reduce the transpiration rate of plants in a short period of time, preventing excessive water loss and protecting cellular water potential [72]. As predicted, g_s showed significant differences under varying water supply conditions in this study. However, these differences varied across wheat growth stages. During the jointing and filling stages, wheat grows vigorously and soil moisture uptake increases.

Therefore, under conditions of insufficient water supply, the g_s differences between the irrigation treatments were the most pronounced [29]. This indicates that the g_s of wheat is closely related to the available soil moisture for crops.

In existing studies, such as that by Wang et al. [29], stomatal conductance was used as a marker for crop water diagnostic modeling. Taking the g_s thresholds for different SWSI scenarios and combining them with the g_s prediction model can help managers to design a more rational irrigation management program. Due to soil variability in different regions, determining soil water stress levels based on the current percentage of soil moisture relative to FC is the most common and effective method [35]. According to existing research, the soil volumetric water content for different stress levels should be maintained at less than 50%, 50–60%, 60–70%, 70–80%, and more than 80% of FC, respectively [71]. Therefore, in this study, the SWSI was calculated based on soil water content under different soil water stress levels. This study proposed four soil water stress levels: extreme drought, severe water stress, moderate water stress, slight water stress, and no water stress, with corresponding SWSI values of less than 0.43, 0.43–0.55, 0.55–0.66, 0.66–0.77, more than 0.77, respectively. The g_s thresholds were obtained from the fitting relationship between the SWSI and g_s at different growth stages of wheat (Table 5). Zhou et al. [30] conducted a winter wheat water stress experiment during the flowering stage and found that under 60–80% FC conditions, g_s ranged from 0.26 to 0.29 mol m^{-2} s^{-1}, which is consistent with this study's results. However, different wheat varieties exhibit different degrees of g_s reduction in response to water stress. Li et al. [73] found that drought-resistant wheat varieties are more sensitive to regulating stomata under water stress, having lower stomatal density and a higher unit organ area compared with common varieties. Therefore, the g_s thresholds proposed in this study have limitations and may be influenced by different wheat varieties. In a subsequent study, we will add more wheat varieties to improve our results.

4.2. Correlation Between Vegetation Indices, Texture Features, and g_s in Winter Wheat

Having more independent features in a dataset is crucial for building a stable and adaptable prediction model. Typically, there is significant collinearity among crop vegetation indices. Research indicates that although vegetation indices are collinear, their combination does not affect model variance because this collinearity is structural [74]. However, using only spectral information has limited effectiveness in improving the accuracy of the model, particularly because spectral saturation occurs in later stages of crop growth [75]. This phenomenon was also observed in this study, where the correlation between the vegetation indices and g_s was very strong after the heading stage of wheat, with most correlation coefficients exceeding 0.7. As shown in Figure 9, the correlation of the image texture features from different bands with g_s varied significantly. Among the textural features, MEA exhibited the highest correlation with g_s, whereas after the heading stage, R-Cor exhibited the strongest correlation with g_s. MEA responds to the concentration and local consistency of the gray values of each pixel in the image, which can characterize the uniformity of the canopy leaves and reflect the current water deficit status of the crop. Thus, MEA had a high correlation with g_s in the overall experiments. COR, on the other hand, emphasizes the linear correlation between the gray values of the image pixels, which responds to the change rule of the texture pattern on the surface of the canopy. After the tasseling stage, the canopy state of wheat changed significantly under different water treatments, which may have led to the enhanced ordering of leaf reflectance spectra, thus strengthening the correlation between COR and g_s.

Compared with vegetation indices, texture information in high-resolution digital images better captures the features of the canopy structure [76]. This is because the winter wheat canopy comprises complex elements, such as leaves, stems, spikes, soil, and shadows, and high-frequency information in texture images can reflect plant vigor [77]. Adequate soil moisture results in more vigorous crops. The study by Wang et al. [25] demonstrated that using a single type of feature (vegetation index) provides a limited improvement in model accuracy, whereas combining remote sensing indices (vegetation index and texture features)

yields better prediction accuracy. Therefore, using multispectral and texture information for feature fusion in this study was reasonable and reliable.

4.3. Accuracy Comparison Between Single Learner and Stacking Ensemble Learning Models in Winter Wheat Water Stress

Different irrigation levels resulted in varied plant growth performance at different growth stages. These physiological parameters have complex relationships with crop canopy spectral and textural information. Compared with traditional linear models, nonlinear machine learning models exhibit superior performance [78]. Herein, the nonlinear machine learning models (RF, SVM, and XGBoost) performed well, but their accuracies varied across the growth stages. The prediction accuracy was the highest after the heading stage, which is consistent with the findings of Wang et al. [29]. This may be because of the growth characteristics and cumulative effects of winter wheat. In the early growth stages, soil moisture is not yet depleted to low levels, resulting in smaller differences in plant physiological parameters between treatments. This reduces model diversity and lowers prediction accuracy. When wheat is subjected to different irrigation treatments over a longer period, the cumulative effect of water deficit leads to increasingly significant phenotypic differences. The correlation between spectral indices, image texture, and g_s reached higher levels, and the model's data source coverage was extensive, enhancing prediction accuracy. This is consistent with the results of Ma et al. [12]. Among the different base learners, XGBoost generally performed better, with R^2 improvements ranging from 4.13% to 8.72% (except during the heading stage). This result can be attributed to XGBoost's nature as a GBDT model, which incrementally adds trees, with each tree learning the residuals of the previous tree's predictions, gradually reducing model bias. In addition, because XGBoost uses regularization terms to optimize the objective function, it reduces the risk of overfitting and improves model stability and accuracy. Similar findings were reported in the studies by Tunca et al. [79] and Zhang et al. [80].

It should be acknowledged that, although certain algorithms exhibit good performance, a single model is insufficient to handle the complexity of various application environments and datasets. For instance, herein, XGBoost did not show a significant improvement in prediction accuracy compared with the other models during the heading stage of the wheat. The SEL model combines different base learners to emphasize their strengths and minimize their weaknesses, thereby producing a strong learner that is significantly better than individual learners [81]. Herein, RF, SVM, and XGBoost were used as base models to establish a g_s prediction model using SEL. The SEL model improved the R^2 by 6.25–14.63% compared with the three base learners. Yang et al. [35] constructed an SEL model for soil moisture prediction using five base learners, and the results showed that the SEL model achieved different degrees of improvement in R^2 compared with the base learners, consistent with our findings. The risk of overfitting is usually present during model training. Although we used K-fold cross-validation to mitigate this risk, it is still necessary to test the SEL model's predictive performance using an independent reserved test set not involved in the model training. Wu et al. [15] reported that when training data samples are limited, an SEL model can achieve higher prediction accuracy, with validation performed using a reserved test set. The test results indicated that the SEL model adapted well to different environments. For example, during the jointing stage, the prediction accuracy of the three base learners varied significantly, but the stacking ensemble model maintained good accuracy by leveraging the strengths of the different models, which is consistent with the results of Tao et al. [32].

Due to the large number of candidate models, verifying all possible combinations of ensemble models is challenging given the constraints of time and computational costs. Therefore, determining the optimal combination of base learners for the SEL model remains a significant challenge. In future research, we will explore more base model combinations to refine the accuracy of the SEL model. Additionally, the climate of different regions and various wheat varieties may affect the accuracy of the models used in this study.

Future research should attempt to introduce data from more regions and wheat varieties to enhance the simulation accuracy and applicability of the SEL model. This research provides a solution for large-scale monitoring of crop water status, assisting agricultural managers in dividing zones with varying water requirements more effectively. Overall, this research provides water decision support for digital agriculture and advances precision agriculture.

5. Conclusions

Water stress in winter wheat at different growth stages was detected using multispectral and image texture data obtained from UAVs combined with SEL algorithms. This study found significant differences in g_s across different growth stages of winter wheat under various irrigation treatments. Linear fitting relationships between g_s and the SWSI were established for the different growth stages, with R^2 values of more than 0.79 indicating high fitting accuracy. Our study demonstrated that g_s could serve as an indicator of soil water stress levels, and based on this, g_s thresholds for different water stress levels were proposed. Furthermore, we constructed an SEL model using three base learners (RF, SVM, and XGBoost) and evaluated the model's performance. The SEL model showed higher prediction accuracy, with R^2 improvements ranging from 6.25% to 14.63%, compared with the three base learners across different growth stages. The model was validated using a reserved test set, achieving R^2 values of 0.798, 0.757, 0.799, 0.688, and 0.867 for the greening, jointing, heading, flowering, and filling stages of winter wheat, respectively. This indicates that the SEL model had sufficient stability and high accuracy. In summary, this study developed a novel method that combines multifeature information fusion with SEL models based on UAV remote sensing technology. The SEL model improved the g_s prediction accuracy, thus obtaining precise g_s thresholds under different soil moisture stresses, which provides a new approach for researching winter wheat water stress and irrigation scheduling.

Author Contributions: Conceptualization, H.Z.; Data curation, H.Z. and J.G.; Formal analysis, J.G. and X.H.; Funding acquisition, H.Y.; Investigation, D.C.; Methodology, H.Z.; Project administration, H.Y.; Resources, H.Z.; Software, H.Z.; Validation, J.W.; Visualization, Y.W.; Writing—original draft, H.Z.; Writing—review & editing, H.Y. All authors have read and agreed to the published version of the manuscript.

Funding: This research was funded by the Key Research and Development Program of Hebei Province (Grant No. 21327002D), the Water Conservancy Technology Demonstration Project of China (Grant No. SF-202311), the Key Research and Development Program of Shandong Province (Grant No. 2022CXGC020707), the National Key Research and Development Program of China (Grant No. 2023YFD1900704), and the China Agriculture Research System (Grant No. CARS-03).

Data Availability Statement: The authors confirm that the data supporting the findings of this study are available within the article.

Conflicts of Interest: The authors declare no conflicts of interest.

References

1. Thapa, S.; Xue, Q.; Jessup, K.E.; Rudd, J.C.; Liu, S.; Marek, T.H.; Devkota, R.N.; Baker, J.A.; Baker, S. Yield Determination in Winter Wheat under Different Water Regimes. *Field Crops Res.* **2019**, *233*, 80–87. [CrossRef]
2. Yan, H.; Hui, X.; Li, M.; Xu, Y. Development in Sprinkler Irrigation Technology in China*. *Irrig. Drain.* **2020**, *69*, 75–87. [CrossRef]
3. Wang, X.; Müller, C.; Elliot, J.; Mueller, N.D.; Ciais, P.; Jägermeyr, J.; Gerber, J.; Dumas, P.; Wang, C.; Yang, H.; et al. Global Irrigation Contribution to Wheat and Maize Yield. *Nat. Commun.* **2021**, *12*, 1235. [CrossRef] [PubMed]
4. Zhao, W.; Liu, L.; Shen, Q.; Yang, J.; Han, X.; Tian, F.; Wu, J. Effects of Water Stress on Photosynthesis, Yield, and Water Use Efficiency in Winter Wheat. *Water* **2020**, *12*, 2127. [CrossRef]
5. Fang, Y.; Du, Y.; Wang, J.; Wu, A.; Qiao, S.; Xu, B.; Zhang, S.; Siddique, K.H.M.; Chen, Y. Moderate Drought Stress Affected Root Growth and Grain Yield in Old, Modern and Newly Released Cultivars of Winter Wheat. *Front. Plant Sci.* **2017**, *8*, 672. [CrossRef]
6. Istiak, M.d.A.; Syeed, M.M.M.; Hossain, M.S.; Uddin, M.F.; Hasan, M.; Khan, R.H.; Azad, N.S. Adoption of Unmanned Aerial Vehicle (UAV) Imagery in Agricultural Management: A Systematic Literature Review. *Ecol. Inform.* **2023**, *78*, 102305. [CrossRef]
7. Zhang, L.; Zhang, H.; Niu, Y.; Han, W. Mapping Maize Water Stress Based on UAV Multispectral Remote Sensing. *Remote Sens.* **2019**, *11*, 605. [CrossRef]

8. Bertalan, L.; Holb, I.; Pataki, A.; Négyesi, G.; Szabó, G.; Kupásné Szalóki, A.; Szabó, S. UAV-Based Multispectral and Thermal Cameras to Predict Soil Water Content—A Machine Learning Approach. *Comput. Electron. Agric.* **2022**, *200*, 107262. [CrossRef]
9. Wang, N.; Clevers, J.G.P.W.; Wieneke, S.; Bartholomeus, H.; Kooistra, L. Potential of UAV-Based Sun-Induced Chlorophyll Fluorescence to Detect Water Stress in Sugar Beet. *Agric. For. Meteorol.* **2022**, *323*, 109033. [CrossRef]
10. Zhang, L.; Han, W.; Niu, Y.; Chávez, J.L.; Shao, G.; Zhang, H. Evaluating the Sensitivity of Water Stressed Maize Chlorophyll and Structure Based on UAV Derived Vegetation Indices. *Comput. Electron. Agric.* **2021**, *185*, 106174. [CrossRef]
11. Sharma, V.; Honkavaara, E.; Hayden, M.; Kant, S. UAV Remote Sensing Phenotyping of Wheat Collection for Response to Water Stress and Yield Prediction Using Machine Learning. *Plant Stress* **2024**, *12*, 100464. [CrossRef]
12. Ma, J.; Liu, B.; Ji, L.; Zhu, Z.; Wu, Y.; Jiao, W. Field-Scale Yield Prediction of Winter Wheat under Different Irrigation Regimes Based on Dynamic Fusion of Multimodal UAV Imagery. *Int. J. Appl. Earth Obs. Geoinf.* **2023**, *118*, 103292. [CrossRef]
13. Bai, Y.; Li, X.; Liu, S.; Wang, P. Modelling Diurnal and Seasonal Hysteresis Phenomena of Canopy Conductance in an Oasis Forest Ecosystem. *Agric. For. Meteorol.* **2017**, *246*, 98–110. [CrossRef]
14. Jones, H.G. *Plants and Microclimate. A Quantitative Approach to Environmental Plant Physiology*; Cambridge University Press: Cambridge, UK, 1983. [CrossRef]
15. Wu, T. Evaluation of Stacking and Blending Ensemble Learning Methods for Estimating Daily Reference Evapotranspiration. *Comput. Electron. Agric.* **2021**, *184*, 106039. [CrossRef]
16. Mira-García, A.B.; Romero-Trigueros, C.; Gambín, J.M.B.; Sánchez-Iglesias, M.D.P.; Tortosa, P.A.N.; Nicolás, E.N. Estimation of Stomatal Conductance by Infra-Red Thermometry in Citrus Trees Cultivated under Regulated Deficit Irrigation and Reclaimed Water. *Agric. Water Manag.* **2023**, *276*, 108057. [CrossRef]
17. Mahdavi, S.; Arzani, A.; Maibody, S.A.M.M.; Mehrabi, A.A. Photosynthetic and Yield Performance of Wheat (*Triticum aestivum* L.) under Sowing in Hot Environment. *Acta Physiol. Plant.* **2021**, *43*, 106. [CrossRef]
18. Liu, E.K.; Mei, X.R.; Yan, C.R.; Gong, D.Z.; Zhang, Y.Q. Effects of water stress on photosynthetic characteristics, dry matter translocation and WUE in two winter wheat genotypes. *Agric. Water Manag.* **2016**, *167*, 75–85. [CrossRef]
19. Greaves, H.E.; Vierling, L.A.; Eitel, J.U.H.; Boelman, N.T.; Magney, T.S.; Prager, C.M.; Griffin, K.L. Estimating Aboveground Biomass and Leaf Area of Low-Stature Arctic Shrubs with Terrestrial LiDAR. *Remote Sens. Environ.* **2015**, *164*, 26–35. [CrossRef]
20. Lee, C.-H.; Chen, K.-Y.; Liu, L.D. Effect of Texture Feature Distribution on Agriculture Field Type Classification with Multitemporal UAV RGB Images. *Remote Sens.* **2024**, *16*, 1221. [CrossRef]
21. Khojastehnazhand, M.; Roostaei, M. Classification of Seven Iranian Wheat Varieties Using Texture Features. *Expert Syst. Appl.* **2022**, *199*, 117014. [CrossRef]
22. Feng, Q.; Liu, J.; Gong, J. UAV Remote Sensing for Urban Vegetation Mapping Using Random Forest and Texture Analysis. *Remote Sens.* **2015**, *7*, 1074–1094. [CrossRef]
23. Kwak, G.-H.; Park, N.-W. Impact of Texture Information on Crop Classification with Machine Learning and UAV Images. *Appl. Sci.* **2019**, *9*, 643. [CrossRef]
24. Wang, F.; Yi, Q.; Hu, J.; Xie, L.; Yao, X.; Xu, T.; Zheng, J. Combining Spectral and Textural Information in UAV Hyperspectral Images to Estimate Rice Grain Yield. *Int. J. Appl. Earth Obs. Geoinf.* **2021**, *102*, 102397. [CrossRef]
25. Wang, R.; Tuerxun, N.; Zheng, J. Improved Estimation of SPAD Values in Walnut Leaves by Combining Spectral, Texture, and Structural Information from UAV-Based Multispectral Image. *Sci. Hortic.* **2024**, *328*, 112940. [CrossRef]
26. Wang, X.; Yan, S.; Wang, W.; Yin, L.; Li, M.; Yu, Z.; Chang, S.; Hou, F. Monitoring Leaf Area Index of the Sown Mixture Pasture through UAV Multispectral Image and Texture Characteristics. *Comput. Electron. Agric.* **2023**, *214*, 108333. [CrossRef]
27. Behmann, J.; Mahlein, A.-K.; Rumpf, T.; Roemer, C.; Pluemer, L. A Review of Advanced Machine Learning Methods for the Detection of Biotic Stress in Precision Crop Protection. *Precis. Agric.* **2015**, *16*, 239–260. [CrossRef]
28. Granata, F. Evapotranspiration Evaluation Models Based on Machine Learning Algorithms—A Comparative Study. *Agric. Water Manag.* **2019**, *217*, 303–315. [CrossRef]
29. Wang, J.; Lou, Y.; Wang, W.; Liu, S.; Zhang, H.; Hui, X.; Wang, Y.; Yan, H.; Maes, W.H. A Robust Model for Diagnosing Water Stress of Winter Wheat by Combining UAV Multispectral and Thermal Remote Sensing. *Agric. Water Manag.* **2024**, *291*, 108616. [CrossRef]
30. Zhou, Y.; Lao, C.; Yang, Y.; Zhang, Z.; Chen, H.; Chen, Y.; Chen, J.; Ning, J.; Yang, N. Diagnosis of Winter-Wheat Water Stress Based on UAV-Borne Multispectral Image Texture and Vegetation Indices. *Agric. Water Manag.* **2021**, *256*, 107076. [CrossRef]
31. Pei, S.; Dai, Y.; Bai, Z.; Li, Z.; Zhang, F.; Yin, F.; Fan, J. Improved Estimation of Canopy Water Status in Cotton Using Vegetation Indices along with Textural Information from UAV-Based Multispectral Images. *Comput. Electron. Agric.* **2024**, *224*, 109176. [CrossRef]
32. Tao, S.; Zhang, X.; Feng, R.; Qi, W.; Wang, Y.; Shrestha, B. Retrieving Soil Moisture from Grape Growing Areas Using Multi-Feature and Stacking-Based Ensemble Learning Modeling. *Comput. Electron. Agric.* **2023**, *204*, 107537. [CrossRef]
33. Jiang, H.; Zhang, S.; Yang, Z.; Zhao, L.; Zhou, Y.; Zhou, D. Quality Classification of Stored Wheat Based on Evidence Reasoning Rule and Stacking Ensemble Learning. *Comput. Electron. Agric.* **2023**, *214*, 108339. [CrossRef]
34. Zhai, W.; Li, C.; Cheng, Q.; Ding, F.; Chen, Z. Exploring Multisource Feature Fusion and Stacking Ensemble Learning for Accurate Estimation of Maize Chlorophyll Content Using Unmanned Aerial Vehicle Remote Sensing. *Remote Sens.* **2023**, *15*, 3454. [CrossRef]

35. Yang, N.; Zhang, Z.; Ding, B.; Wang, T.; Zhang, J.; Liu, C.; Zhang, Q.; Zuo, X.; Chen, J.; Cui, N.; et al. Evaluation of Winter-Wheat Water Stress with UAV-Based Multispectral Data and Ensemble Learning Method. *Plant Soil* **2023**, *497*, 647–668. [CrossRef]
36. Shirazi, M.A.; Boersma, L.; Hart, J.W. A Unifying Quantitative Analysis of Soil Texture: Improvement of Precision and Extension of Scale. *Soil Sci. Soc. Am. J.* **1988**, *52*, 181. [CrossRef]
37. Ostu, N. A Threshold Selection Method from Gray-Level Histograms. *IEEE Trans. SMC* **1979**, *9*, 62.
38. Haralick, R.M.; Shanmugam, K.; Dinstein, I.H. Textural Features for Image Classification. *IEEE Trans. Syst. Man Cybern.* **1973**, *SMC-3*, 610–621. [CrossRef]
39. Rouse, J.W.; Haas, R.H.; Schell, J.A.; Deering, D.W. *Monitoring Vegetation Systems in the Great Plains with ERTS*; NASA Special Publication: Washington, DC, USA, 1974.
40. Gitelson, A.A.; Kaufman, Y.J.; Merzlyak, M.N. Use of a Green Channel in Remote Sensing of Global Vegetation from EOS-MODIS. *Remote Sens. Environ.* **1996**, *58*, 289–298. [CrossRef]
41. Liu, H.Q.; Huete, A. A Feedback Based Modification of the NDVI to Minimize Canopy Background and Atmospheric Noise. *IEEE Trans. Geosci. Remote Sens.* **1995**, *33*, 457–465. [CrossRef]
42. Jiang, Z.; Huete, A.R.; Didan, K.; Miura, T. Development of a Two-Band Enhanced Vegetation Index without a Blue Band. *Remote Sens. Environ.* **2008**, *112*, 3833–3845. [CrossRef]
43. Huete, A.R. A Soil-Adjusted Vegetation Index (SAVI). *Remote Sens. Environ.* **1988**, *25*, 295–309. [CrossRef]
44. Rondeaux, G.; Steven, M.; Baret, F. Optimization of Soil-Adjusted Vegetation Indices. *Remote Sens. Environ.* **1996**, *55*, 95–107. [CrossRef]
45. Cao, Q.; Miao, Y.; Feng, G.; Gao, X.; Li, F.; Liu, B.; Yue, S.; Cheng, S.; Ustin, S.L.; Khosla, R. Active Canopy Sensing of Winter Wheat Nitrogen Status: An Evaluation of Two Sensor Systems. *Comput. Electron. Agric.* **2015**, *112*, 54–67. [CrossRef]
46. Daughtry, C.S.; Walthall, C.L.; Kim, M.S.; De Colstoun, E.B.; McMurtrey, J.E., III. Estimating Corn Leaf Chlorophyll Concentration from Leaf and Canopy Reflectance. *Remote Sens. Environ.* **2000**, *74*, 229–239. [CrossRef]
47. Haboudane, D.; Miller, J.R.; Tremblay, N.; Zarco-Tejada, P.J.; Dextraze, L. Integrated Narrow-Band Vegetation Indices for Prediction of Crop Chlorophyll Content for Application to Precision Agriculture. *Remote Sens. Environ.* **2002**, *81*, 416–426. [CrossRef]
48. Haboudane, D.; Miller, J.R.; Pattey, E.; Zarco-Tejada, P.J.; Strachan, I.B. Hyperspectral Vegetation Indices and Novel Algorithms for Predicting Green LAI of Crop Canopies: Modeling and Validation in the Context of Precision Agriculture. *Remote Sens. Environ.* **2004**, *90*, 337–352. [CrossRef]
49. Penuelas, J.; Baret, F.; Filella, I. Semi-Empirical Indices to Assess Carotenoids/Chlorophyll a Ratio from Leaf Spectral Reflectance. *Photosynthetica* **1995**, *31*, 221–230.
50. Fitzgerald, G.; Rodriguez, D. Garry O'Leary Measuring and Predicting Canopy Nitrogen Nutrition in Wheat Using a Spectral Index—The Canopy Chlorophyll Content Index (CCCI). *Field Crops Res.* **2010**, *116*, 318–324. [CrossRef]
51. Sripada, R.P.; Heiniger, R.W.; White, J.G.; Weisz, R. Aerial Color Infrared Photography for Determining Late-Season Nitrogen Requirements in Corn. *Agron. J.* **2005**, *97*, 1443–1451. [CrossRef]
52. Jordan, C.F. Derivation of Leaf-Area Index from Quality of Light on the Forest Floor. *Ecology* **1969**, *50*, 663–666. [CrossRef]
53. Gitelson, A.A.; Viña, A.; Ciganda, V.; Rundquist, D.C.; Arkebauer, T.J. Remote Estimation of Canopy Chlorophyll Content in Crops. *Geophys. Res. Lett.* **2005**, *32*, 2005GL022688. [CrossRef]
54. Broge, N.H.; Mortensen, J.V. Deriving Green Crop Area Index and Canopy Chlorophyll Density of Winter Wheat from Spectral Reflectance Data. *Remote Sens. Environ.* **2002**, *81*, 45–57. [CrossRef]
55. Dash, J.; Curran, P.J. Evaluation of the MERIS Terrestrial Chlorophyll Index. In Proceedings of the IGARSS 2004. 2004 IEEE International Geoscience and Remote Sensing Symposium, Anchorage, AK, USA, 20–24 September 2004; IEEE: Piscataway, NJ, USA, 2004; Volume 1.
56. Elsayed, S.; Rischbeck, P.; Schmidhalter, U. Comparing the Performance of Active and Passive Reflectance Sensors to Assess the Normalized Relative Canopy Temperature and Grain Yield of Drought-Stressed Barley Cultivars. *Field Crops Res.* **2015**, *177*, 148–160. [CrossRef]
57. Goel, N.S.; Qin, W. Influences of Canopy Architecture on Relationships between Various Vegetation Indices and LAI and Fpar: A Computer Simulation. *Remote Sens. Rev.* **1994**, *10*, 309–347. [CrossRef]
58. Metternicht, G. Vegetation Indices Derived from High-Resolution Airborne Videography for Precision Crop Management. *Int. J. Remote Sens.* **2003**, *24*, 2855–2877. [CrossRef]
59. Wang Ke, W.K.; Shen ZhangQuan, S.Z.; Wang RenChao, W.R. Effects of Nitrogen Nutrition on the Spectral Reflectance Characteristics of Rice Leaf and Canopy. *J. Zhejiang Agric. Univ.* **1998**, *24*, 93–97.
60. Diker, K.; Bausch, W.C. Potential Use of Nitrogen Reflectance Index to Estimate Plant Parameters and Yield of Maize. *Biosyst. Eng.* **2003**, *85*, 437–447. [CrossRef]
61. Eitel, J.U.H.; Long, D.S.; Gessler, P.E.; Smith, A.M.S. Using In-situ Measurements to Evaluate the New RapidEye™ Satellite Series for Prediction of Wheat Nitrogen Status. *Int. J. Remote Sens.* **2007**, *28*, 4183–4190. [CrossRef]
62. Broge, N.H.; Leblanc, E. Comparing Prediction Power and Stability of Broadband and Hyperspectral Vegetation Indices for Estimation of Green Leaf Area Index and Canopy Chlorophyll Density. *Remote Sens. Environ.* **2001**, *76*, 156–172. [CrossRef]
63. Jury, W.A.; Horton, R. *Soil Physics*; John Wiley & Sons: Hoboken, NJ, USA, 2004; ISBN 978-0-471-05965-3.

64. Cheng, Q.; Xu, H.; Fei, S.; Li, Z.; Chen, Z. Estimation of Maize LAI Using Ensemble Learning and UAV Multispectral Imagery under Different Water and Fertilizer Treatments. *Agriculture* **2022**, *12*, 1267. [CrossRef]
65. Feng, L.; Li, Y.; Wang, Y.; Du, Q. Estimating Hourly and Continuous Ground-Level $PM_{2.5}$ Concentrations Using an Ensemble Learning Algorithm: The ST-Stacking Model. *Atmos. Environ.* **2020**, *223*, 117242.1–117242.13. [CrossRef]
66. Breiman, L. Breiman Random Forests. *Mach. Learn.* **2001**, *45*, 5–32. [CrossRef]
67. Biau, G.; Scornet, E. A Random Forest Guided Tour. *TEST* **2016**, *25*, 197–227. [CrossRef]
68. Chen, T.; Guestrin, C. XGBoost: A Scalable Tree Boosting System. In Proceedings of the KDD '16: Proceedings of the 22nd ACM SIGKDD International Conference on Knowledge Discovery and Data Mining, San Francisco, CA, USA, 13–17 August 2016. [CrossRef]
69. Porporato, A.; Laio, F.; Ridol, L.; Rodriguez-Iturbe, I. Plants in Water-Controlled Ecosystems: Active Role in Hydrologic Processes and Response to Water Stress III. Vegetation Water Stress. *Adv. Water Resour.* **2001**, *24*, 695–705. [CrossRef]
70. Asargew, M.F.; Masutomi, Y.; Kobayashi, K.; Aono, M. Water Stress Changes the Relationship between Photosynthesis and Stomatal Conductance. *Sci. Total Environ.* **2024**, *907*, 167886. [CrossRef]
71. Chai, Q.; Gan, Y.; Zhao, C.; Xu, H.-L.; Waskom, R.M.; Niu, Y.; Siddique, K.H.M. Regulated Deficit Irrigation for Crop Production under Drought Stress. A Review. *Agron. Sustain. Dev.* **2016**, *36*, 3. [CrossRef]
72. Kang, S.Z.; Zhang, F.C.; Zhang, J.H. A Simulation Model of Water Dynamics in Winter Wheat Field and Its Application in a Semiarid Region. *Agric. Water Manag.* **2001**, *49*, 115–129. [CrossRef]
73. Li, Y.; Li, H.; Li, Y.; Zhang, S. Improving Water-Use Efficiency by Decreasing Stomatal Conductance and Transpiration Rate to Maintain Higher Ear Photosynthetic Rate in Drought-Resistant Wheat. *Crop J.* **2017**, *5*, 231–239. [CrossRef]
74. Siegel, A.F.; Wagner, M.R. Multiple Regression: Predicting One Variable from Several Others. In *Practical Business Statistics*; Academic Press: Cambridge, MA, USA, 2016; pp. 355–418.
75. Liu, F.; Hu, P.; Zheng, B.; Duan, T.; Zhu, B.; Guo, Y. A Field-Based High-Throughput Method for Acquiring Canopy Architecture Using Unmanned Aerial Vehicle Images. *Agric. For. Meteorol.* **2021**, *296*, 108231. [CrossRef]
76. Alzhanov, A.; Nugumanova, A. Crop Classification Using UAV Multispectral Images with Gray-Level Co-Occurrence Matrix Features. *Procedia Comput. Sci.* **2024**, *231*, 734–739. [CrossRef]
77. Schumacher, P.; Mislimshoeva, B.; Brenning, A.; Zandler, H.; Brandt, M.; Samimi, C.; Koellner, T. Do Red Edge and Texture Attributes from High-Resolution Satellite Data Improve Wood Volume Estimation in a Semi-Arid Mountainous Region? *Remote Sens.* **2016**, *8*, 540. [CrossRef]
78. Liu, T.; Xu, T.; Yu, F.; Yuan, Q.; Guo, Z.; Xu, B. A Method Combining ELM and PLSR (ELM-P) for Estimating Chlorophyll Content in Rice with Feature Bands Extracted by an Improved Ant Colony Optimization Algorithm. *Comput. Electron. Agric.* **2021**, *186*, 106177. [CrossRef]
79. Tunca, E.; Köksal, E.S.; Öztürk, E.; Akay, H.; Çetin Taner, S. Accurate Estimation of Sorghum Crop Water Content under Different Water Stress Levels Using Machine Learning and Hyperspectral Data. *Environ. Monit. Assess.* **2023**, *195*, 877. [CrossRef] [PubMed]
80. Zhang, Y.; Xia, C.; Zhang, X.; Cheng, X.; Feng, G.; Wang, Y.; Gao, Q. Estimating the Maize Biomass by Crop Height and Narrowband Vegetation Indices Derived from UAV-Based Hyperspectral Images. *Ecol. Indic.* **2021**, *129*, 107985. [CrossRef]
81. Fu, B.; He, X.; Yao, H.; Liang, Y.; Deng, T.; He, H.; Fan, D.; Lan, G.; He, W. Comparison of RFE-DL and Stacking Ensemble Learning Algorithms for Classifying Mangrove Species on UAV Multispectral Images. *Int. J. Appl. Earth Obs. Geoinf.* **2022**, *112*, 102890. [CrossRef]

Disclaimer/Publisher's Note: The statements, opinions and data contained in all publications are solely those of the individual author(s) and contributor(s) and not of MDPI and/or the editor(s). MDPI and/or the editor(s) disclaim responsibility for any injury to people or property resulting from any ideas, methods, instructions or products referred to in the content.